Sublattice-enriched tunability of bound states in second-order topological insulators and superconductors

Di Zhu,[1] Majid Kheirkhah,[2,3] and Zhongbo Yan[1,*]

[1]*Guangdong Provincial Key Laboratory of Magnetoelectric Physics and Devices, School of Physics, Sun Yat-Sen University, Guangzhou 510275, China*

[2]*Department of Physics, University of Alberta, Edmonton, Alberta T6G 2E1, Canada*

[3]*Department of Physics, Simon Fraser University, Burnaby, British Columbia V5A 1S6, Canada*

(Received 20 November 2022; revised 1 February 2023; accepted 3 February 2023; published 9 February 2023)

Bound states at sharp corners have been widely viewed as the hallmark of two-dimensional second-order topological insulators and superconductors. In this paper, we show that the existence of sublattice degrees of freedom can enrich the tunability of bound states on the boundary and hence lift the constraint on their locations. We take the Kane-Mele model with honeycomb-lattice structure to illustrate the underlying physics. With the introduction of an in-plane exchange field to the model, we find that the boundary Dirac mass induced by the exchange field has a sensitive dependence on the boundary sublattice termination. We find that the sensitive sublattice dependence can lead bound states to emerge at a specific type of boundary defects named as sublattice domain walls if the exchange field is of ferromagnetic nature, even in the absence of any sharp corner on the boundary. Remarkably, this sensitive dependence of the boundary Dirac mass on the boundary sublattice termination allows the positions of bound states to be manipulated to any place on the boundary for an appropriately-designed sample. With a further introduction of conventional s-wave superconductivity to the model, we find that, no matter whether the exchange field is ferromagnetic, antiferromagnetic, or ferrimagnetic, highly controllable Majorana zero modes can be achieved at the sublattice domain walls. Our paper reshapes the understanding of boundary physics in second-order topological phases, and meanwhile opens potential avenues to realize highly controllable bound states for potential applications.

DOI: 10.1103/PhysRevB.107.085407

I. INTRODUCTION

Since the discovery of two-dimensional (2D) topological insulators (TIs) [1–5], an enduring and intensive exploration of topological phases in quantum materials as well as various classical systems has been witnessed [6–9]. A hallmark of topological phases is the existence of gapless states on the boundary enforced by the bulk topological invariant [10]. Conventionally, the gapless states are known to be distributed on the boundary with the dimension lower than the bulk by one. In other words, the gapless boundary states have codimension $d_c = 1$. Recently, it has been uncovered that there in fact exists a large class of topological phases whose gapless boundary states have $d_c \geqslant 2$ [11–31]. For distinction, now a topological phase is dubbed as an nth-order topological phase if it only supports gapless boundary states with $d_c = n$ [32–34].

Different orders of topological phases have a hierarchy connection [35]. In principle, an nth-order topological phase could be descended from an $(n-1)$th-order topological phase by appropriately lifting the protecting symmetry. A paradigmatic example is the realization of a second-order TI by lifting the time-reversal symmetry of a first-order TI [11,12,36–38]. The physics behind such a transition can be intuitively understood via the Jackiw-Rebbi theory based on low-energy boundary Dirac-Hamiltonians [32,33,39]. That is, the breaking of time-reversal symmetry, e.g., by applying a magnetic field, will introduce a boundary Dirac mass to gap out the helical boundary (surface or edge) states, leading to a trivialization of the first-order topological insulating phase [40]. Interestingly, the induced Dirac mass generally shows a dependence on the orientation of the boundary and may change sign across some direction [21]. When the Dirac masses on two boundaries with different orientations have opposite signs, a Dirac-mass domain wall harboring gapless states with $d_c = 2$ will be formed at their intersection [39], a corner in 2D [36–38,41,42], or a hinge in 3D [11,12,43–45]. Because of the generality of this domain-wall picture, bound states positioned at corners in 2D systems [46–52] and chiral or helical states propagating along hinges in 3D systems [53–58] have been widely taken as the defining boundary characteristic of second-order topology.

When the sign of the boundary Dirac mass for a given system is only sensitive to the orientation of the boundary, e.g., a higher-order topological phase enforced by mirror symmetry [17,20], it is true that the bound states will be strongly bounded at sharp corners or hinges where the orientation of the boundary has a dramatic change. However, if the boundary Dirac mass is also sensitive to other factors on the boundary, then it is possible that the bound states are not necessarily pinned at sharp corners or hinges, but instead are allowed to be positioned anywhere on the boundary. Obviously, the tunability of bound states could make the observation of many interesting phenomena possible, such as the creation of additional bound states or the annihilation of bound states.

*yanzhb5@mail.sysu.edu.cn

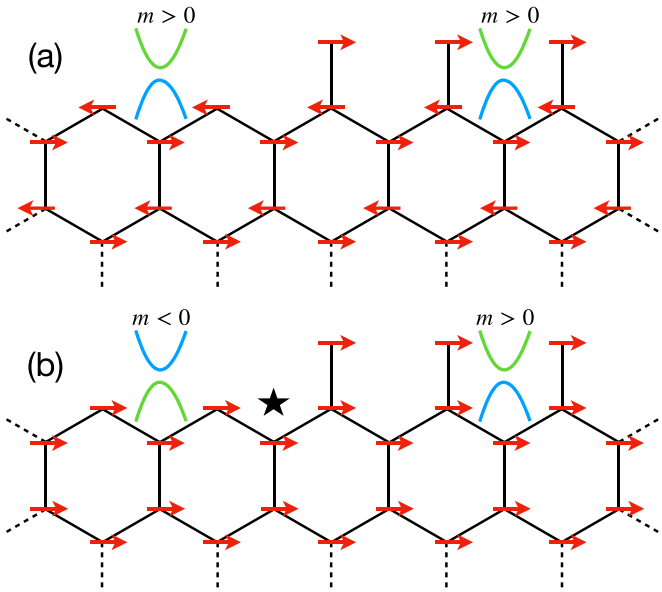

FIG. 1. A schematic diagram of the sublattice domain walls and the dependence of boundary Dirac mass (m) on the sublattice termination. The upper boundary consists of two parts, with one part being a zigzag edge (top left-hand side in each panel) and the other being a beard edge (top right-hand side in each panel), leading to the formation of sublattice domain walls at their intersections. The blue and green parabolas represent massive Dirac energy spectra of the gapped edge states. Different color patterns are just used to intuitively illustrate whether the signs of Dirac masses on the two sides of the sublattice domain wall are the same (a) or opposite (b). On each site, the red arrow denotes the direction of the exchange field. (a) When the exchange field is antiferromagnetic, the boundary Dirac masses on the upper zigzag and beard edges have the same sign, accordingly, the sublattice domain wall is not a Dirac-mass domain wall and hence does not harbor any bound states. (b) When the exchange field is ferromagnetic, the boundary Dirac masses on the upper zigzag and beard edges have opposite signs, hence the sublattice domain wall is a Dirac-mass domain wall supporting bound state illustrated by the black star.

Recently, we did find that the sign of boundary Dirac mass in systems with sublattice degrees of freedom can have a sensitive dependence on the boundary sublattice termination in the context of second-order topological superconductors (TSCs) [59,60]. Concretely, we found that when a 2D first-order TI with honeycomb [59] or kagome lattice structure [60] is placed on an unconventional superconductor, e.g., a d-wave superconductor, the Dirac mass induced by superconductivity gapping out the helical edge states exhibits a sensitive dependence on the type of terminating sublattices on the boundary. This property allows the realization of Majorana Kramers pairs (a Majorana Kramers pair corresponds to two Majorana zero modes (MZMs) related by time-reversal symmetry [61]) at the so-called sublattice domain walls, a type of boundary defects corresponding to the intersection of two edges with the same orientation but with different sublattice terminations, see illustration in Fig. 1. Remarkably, the Majorana Kramers pairs with $d_c = 2$ can emerge even without the existence of sharp corners (e.g., a cylindrical geometry with one direction being periodic) [59], and their positions can be manipulated by tuning the sublattice terminations [59,60], which may benefit the future application of Majorana bound states in topological quantum computation [62–65].

It is known that when the time-reversal symmetry is broken, the helical boundary states of a first-order TI would be gapped out [7,66]. The time-reversal symmetry could be broken by an exchange field, which itself could be induced by an emergent intrinsic magnetic order or magnetic proximity effect from a substrate magnetic insulator. As Dirac domain walls can exist in both superconductors and insulators, it is natural to expect that the Dirac mass induced by exchange field may also have similar sensitive dependence on the sublattice termination, and the realization of bound states at sublattice domain walls may also occur in the context of second-order TIs. In this paper, we take the paradigmatic Kane-Mele model with honeycomb lattice structure to demonstrate this expectation [1,2]. The Kane-Mele model is known to support first-order topological insulating phase, and the honeycomb lattice contains only two sublattice degrees of freedom (labeled as A and B for discussion). Following previous works, we consider that the exchange field lies in the lattice plane [36,37], and for generality we consider that the collinear magnetic moments on the two types of sublattices satisfy $\boldsymbol{M}_A = \gamma \boldsymbol{M}_B$ with $-1 \leqslant \gamma \leqslant 1$. Correspondingly, $0 \leqslant \gamma \leqslant 1$ refers to a ferromagnetic order, $\gamma = -1$ refers to an antiferromagnetic order, and $-1 < \gamma < 0$ refers to a ferrimagnetic order. Based on the low-energy edge theory [22,59], we determine the boundary Dirac masses on the two types of edges whose terminations contain only one type of sublattices (commonly dubbed zigzag and beard edges [67]).

Our main findings can be briefly summarized as follows. First, we find that, for the zigzag and beard edges with the same orientation, whether the values or signs of the Dirac masses on them are the same or not depends on the value of γ. Somewhat counterintuitively, we find that, for an antiferromagnetic or ferrimagnetic exchange field, i.e., $-1 \leqslant \gamma < 0$, the Dirac masses on them take the same sign, even though the directions of the exchange field are opposite on the outermost terminating sublattices for these two kinds of edges, as depicted in Fig. 1(a). On the contrary, for a ferromagnetic exchange field, we find that the Dirac masses on them take opposite signs, even though the directions of the exchange field are the same on the outermost terminating sublattices for these two kinds of edges, as depicted in Fig. 1(b). Because of the sign difference in Dirac masses, we find that the ferromagnetic exchange field can induce highly controllable bound states at the sublattice domain walls corresponding to the intersection of zigzag and beard edges. As an important consequence, bound states can be achieved even in the absence of any sharp corner on the boundary. As the boundary Dirac mass induced by exchange field and the effective chemical potential on the boundary turn out to have a sensitive dependence on the sublattice terminations, we show that these properties allows the realization of MZMs at the sublattice domain walls even one considers conventional s-wave superconductivity, which, in the absence of exchange field, will introduce a uniform boundary Dirac mass [59]. Our findings suggest that the ubiquitous sublattice degrees of freedom in materials provide a knob to control and manipulate the positions of bound states in second-order topological phases.

This paper is organized as follows. In Sec. II, we introduce the Hamiltonian describing a first-order TI subjected to an in-plane exchange field. In Sec. III, we establish a theory distinct from the one developed by Ren *et al.* [36] to understand the robustness of helical edge states on the armchair edges, and show that the helical edge states on the armchair edges will be gapped out once the exchange fields on the two sublattices are different, leading to the presence of corner bound states in samples with geometries different from the one with diamond shape considered in Ref. [36]. In Sec. IV, we derive the low-energy boundary Hamiltonians on the beard and zigzag edges, and show explicitly the dependence of boundary Dirac masses on the sublattice terminations. The presence of bound states at the sublattice domain walls is also numerically demonstrated. In Sec. V, we further consider the introduction of s-wave superconductivity to the system and show the presence of MZMs at the sublattice domain walls. We discuss the results and conclude the paper in Sec. VI. Some calculating details of the low-energy boundary Hamiltonians are relegated to appendices.

II. KANE-MELE MODEL WITH AN IN-PLANE EXCHANGE FIELD

We start with the Hamiltonian [1,2]

$$H = t\sum_{\langle ij\rangle,\alpha} c^{\dagger}_{i,\alpha}c_{j,\alpha} + i\lambda_{\rm so}\sum_{\langle\langle ij\rangle\rangle,\alpha,\beta} \nu_{ij}c^{\dagger}_{i,\alpha}(s_z)_{\alpha\beta}c_{j,\beta} + \lambda_v\sum_{i,\alpha}\xi_i c^{\dagger}_{i,\alpha}c_{i,\alpha} + \sum_{i,\alpha,\beta} c^{\dagger}_{i,\alpha}(\boldsymbol{M}_i\cdot\mathbf{s})_{\alpha\beta}c_{i,\beta}, \quad (1)$$

where $c^{\dagger}_{i,\alpha}$ ($c_{i,\alpha}$) refers to a fermion creation (annihilation) operator at site i, the subscripts α and β refer to spin indices, t denotes the hopping energy, $\lambda_{\rm so}$ characterizes the strength of intrinsic spin-orbit coupling, $\nu_{ij} = 1(-1)$ for a clockwise (anticlockwise) path along which the electrons hop from site j to site i, λ_v characterizes the staggered sublattice potential ($\xi_i = \pm 1$), and the last term describes the exchange field induced by certain collinear magnetic order (the involving g factor and $\hbar$ are made implicity for notational simplicity). The notations $\langle ij\rangle$ and $\langle\langle ij\rangle\rangle$ mean that the sum is over nearest-neighbor sites and next-nearest-neighbor sites, respectively. As in this paper we are interested in second-order topology, the collinear magnetic order will be assumed to lie in the lattice plane, i.e., $\boldsymbol{M}_{i\in A} = \boldsymbol{M} = (M_x, M_y, 0)$, and for generality we consider $\boldsymbol{M}_{i\in B} = \gamma\boldsymbol{M}$ with $-1 \leqslant \gamma \leqslant 1$ to take all possible in-plane collinear magnetic orders into account.

By performing a Fourier transformation and choosing the basis to be $\psi_k = (c_{k,A,\uparrow}, c_{k,B,\uparrow}, c_{k,A,\downarrow}, c_{k,B,\downarrow})^T$, the Hamiltonian in momentum space reads

$$\mathcal{H}(\boldsymbol{k}) = t\sum_{i=1}^{3}[\cos(\boldsymbol{k}\cdot\boldsymbol{a}_i)s_0\sigma_x + \sin(\boldsymbol{k}\cdot\boldsymbol{a}_i)s_0\sigma_y] + 2\lambda_{\rm so}\sum_{i=1}^{3}\sin(\boldsymbol{k}\cdot\boldsymbol{b}_i)s_z\sigma_z + \lambda_v s_0\sigma_z + \frac{1+\gamma}{2}(\boldsymbol{M}\cdot\mathbf{s})\sigma_0 + \frac{1-\gamma}{2}(\boldsymbol{M}\cdot\mathbf{s})\sigma_z, \quad (2)$$

where the Pauli matrices s_i and σ_i, and the identity matrices s_0 and σ_0, act on the spin ($\uparrow,\downarrow$) and sublattice (A,B) degrees of freedom, respectively. $\boldsymbol{a}_i$ refers to the nearest-neighbor vectors, with $\boldsymbol{a}_1 = a(0,1)$, $\boldsymbol{a}_2 = \frac{a}{2}(\sqrt{3},-1)$, $\boldsymbol{a}_3 = \frac{a}{2}(-\sqrt{3},-1)$ (throughout the paper we set the lattice constant $a = 1$ for notational simplicity). The next-nearest-neighbor vectors $\boldsymbol{b}_1 = \boldsymbol{a}_2 - \boldsymbol{a}_3$, $\boldsymbol{b}_2 = \boldsymbol{a}_3 - \boldsymbol{a}_1$ and $\boldsymbol{b}_3 = \boldsymbol{a}_1 - \boldsymbol{a}_2$ [68]. The last line in (2) means that a general collinear exchange field can be decomposed as the sum of a uniform ferromagnetic exchange field and an antiferromagnetic one. Without the two time-reversal-symmetry-breaking terms in the last line, the Hamiltonian describes a first-order TI when $|\lambda_v| < 3\sqrt{3}|\lambda_{\rm so}|$ [2].

III. HELICAL EDGE STATES AND CORNER BOUND STATES ON THE BOUNDARY

Considering the Kane-Mele model with only the ferromagnetic term, Ren *et al.* showed that the helical edge states would be gapped out on the zigzag edges, but remain gapless on the armchair edges [36], irrespective of the direction of the in-plane ferromagnetic exchange field. In order to avoid gapless edge states with codimension $d_c = 1$ and only have bound states with $d_c = 2$ on the boundary, Ren *et al.* suggested a diamond-shaped nanoflake with only zigzag boundaries. For such a geometry, they showed that helical edge states are gapped out on all edges, while bound states show up at half of the corners [36]. By a close look of the Fig. 1 therein, one can notice that these corners hosting bound states correspond to the intersections of two adjacent zigzag edges with different orientations as well as distinct sublattice terminations.

In Ref. [36], the reason that the helical edge states are stable against the in-plane exchange field (corresponding to $\gamma = 1$) was attributed to the existence of an additional mirror symmetry on the armchair edges, which provides a further protection. In more detail, it is known that k_y remains a good quantum number on the armchair edges if periodic boundary conditions are imposed in the y direction. In Ref. [36], the authors considered the limit without the staggered sublattice potential, i.e., $\lambda_v = 0$, and found that the reduced Hamiltonian $\mathcal{H}(k_x, k_y = 0)$ has a mirror symmetry, with the symmetry operator taking the general form $\mathcal{M}_n = i(\hat{\boldsymbol{n}}\cdot\mathbf{s})\sigma_x$, where $\hat{\boldsymbol{n}}$ denotes the direction of the magnetic moment. As $[\mathcal{H}(k_x,0), \mathcal{M}_n] = 0$, $\mathcal{H}(k_x,0)$ can be decomposed as a direct sum of two sectors for any k_x according to the two eigenvalues ($\pm i$) of the mirror operator, and it turns out that the two sectors carry opposite winding numbers, $\omega^{\pm i} = \pm 1$. Although this explanation is valid in the limit with $\lambda_v = 0$, it is in fact not essential. To see this, we would like to point out that the helical edge states in fact remain gapless when $\lambda_v \neq 0$, as long as the exchange field has the same value on the two types of sublattices, i.e., $\gamma = 1$, as shown in Figs. 2(a) and 2(b). However, once $\lambda_v \neq 0$, the aforementioned mirror symmetry is explicitly broken by the staggered sublattice potential (note $[\lambda_v s_0\sigma_z, \mathcal{M}_n] \neq 0$). Accordingly, the Hamiltonian can no longer be decomposed into two mirror sectors, and the topological analysis based on the mirror-graded winding numbers in Ref. [36] breaks down. Nevertheless, the robustness of the crossing at $k_y = 0$ on the armchair edges even when $\lambda_v \neq 0$ suggests the existence of a topological protection.

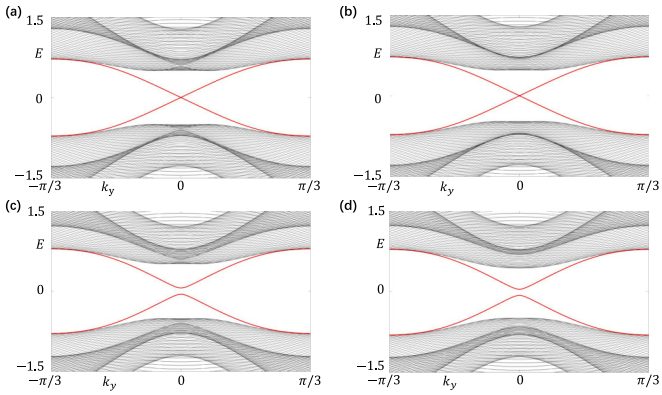

FIG. 2. Energy spectra for a ribbon with armchair edges. The ribbon has open boundary conditions in the x direction and periodic boundary conditions in the y direction. Chosen parameters are $t = 1$, $\lambda_{so} = 0.1$, $M_x = M_y = 0.2$. (a) $\lambda_v = 0$, $\gamma = 1$, (b) $\lambda_v = 0.1$, $\gamma = 1$, (c) $\lambda_v = 0$, $\gamma = 0.5$, and (d) $\lambda_v = 0.1$, $\gamma = 0.5$.

Viewing $\mathcal{H}(k_x, 0)$ as a one-dimensional Hamiltonian, the double degeneracy of the crossing on one armchair edge suggests the existence of two zero-energy bound states at each end of the one-dimensional system. As the spinful time-reversal symmetry is explicitly broken by the exchange field, it is known that in one dimension only chiral symmetry can protect the existence of two degenerate bound states at the same end [69,70]. We find that the chiral symmetry operator for the one-dimensional Hamiltonian $\mathcal{H}(k_x, 0)$ has the form $\mathcal{C} = s_z\sigma_y$. Accordingly, one can define a winding number to characterize the full Hamiltonian $\mathcal{H}(k_x, 0)$. The winding number is given by [71]

$$\omega = \frac{1}{2\pi i}\int_{BZ} dk_x \mathrm{Tr}[Q^{-1}(k_x)\partial_{k_x}Q(k_x)], \tag{3}$$

where "BZ" stands for Brillouin zone, "Tr" stands for the trace operation, and $Q(k_x)$ is related to the Hamiltonian and determined by rewriting the Hamiltonian into a new basis under which the chiral symmetry operator is diagonal, i.e., $\tilde{\mathcal{C}} = \mathrm{diag}\{1, 1, -1, -1\}$, correspondingly,

$$\tilde{\mathcal{H}}(k_x, 0) = \begin{pmatrix} 0 & Q(k_x) \\ Q^\dagger(k_x) & 0 \end{pmatrix}. \tag{4}$$

Here the explicit form of $Q(k_x)$ is

$$Q(k_x) = \begin{pmatrix} M_x - iM_y & F(k_x) - i\lambda_v \\ F(k_x) + i\lambda_v & M_x + iM_y \end{pmatrix}, \tag{5}$$

where $F(k_x) = t[2\cos(\frac{\sqrt{3}}{2}k_x) + 1] - i2\lambda_{so}[\sin(\sqrt{3}k_x) - 2\sin(\frac{\sqrt{3}}{2}k_x)]$. Since the chiral symmetry is preserved even when λ_v, M_x, and M_y are all nonzero, the topological invariant will hold its value as long as the bulk energy gap of $\mathcal{H}(k_x, 0)$ remains open, therefore, the winding number can be determined by considering the limit with $\lambda_v = M_x = M_y = 0$. Accordingly, it is easy to find that

$$\omega = \frac{1}{2\pi i}\int_{BZ} dk_x 2F^{-1}(k_x)\partial_{k_x}F(k_x) = 2. \tag{6}$$

The chiral symmetry and the value of the winding number explain the robustness of the doubly-degenerate crossing of the helical edge states on the armchair edges even when $\lambda_v \neq 0$.

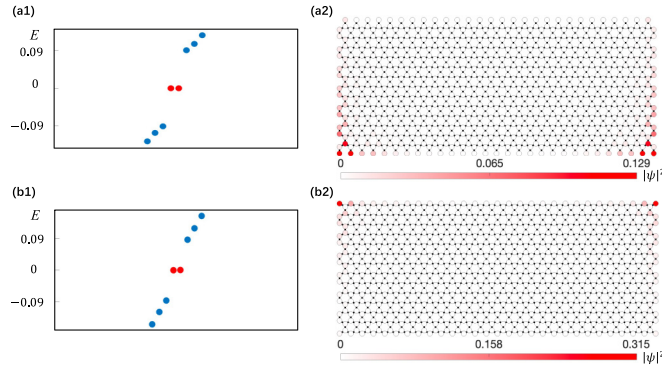

FIG. 3. Corner bound states in a rectangular sample with both x and y directions taking open boundary conditions. Chosen parameters are $t = 1$, $\lambda_{so} = 0.1$, $M_x = M_y = 0.2$, $\gamma = 0.3$, $\lambda_v = 0$, and $N_x = N_y = 28$. The geometries of the samples are depicted in (a2) and (b2), and a few corresponding eigenenergies near zero energy are shown in (a1) and (b1). The red dots in (a1) and (b1) correspond to the eigenenergies of the corner bound states. The shade of the red color on the lattice sites in (a2) and (b2) reflects the weight of the probability density of the corner bound states.

When $\gamma \neq 1$, it is easy to find that the antiferromagnetic term in Hamiltonian (2) commutes with the chiral symmetry operator, i.e., $[(\boldsymbol{M}\cdot\mathbf{s})\sigma_z, \mathcal{C}] = 0$, indicating that the antiferromagnetic term breaks the chiral symmetry of $\mathcal{H}(k_x, 0)$. As a result, the protection of the crossing at $k_y = 0$ from the chiral symmetry is lifted and the helical edge states on the armchair edges would be gapped out by the antiferromagnetic term. As shown in Figs. 2(c) and 2(d), the numerical results confirm this expectation, reflecting the correctness of our analysis.

The opening of an energy gap to the helical edge states on the armchair edges implies an important consequence: One no longer needs to avoid the armchair edges to achieve corner bound states. Now bound states are also possible to emerge at the corners corresponding to the intersections of armchair edges and other types of edges, such as zigzag or beard edges. By numerical calculations, we confirm this expectation, as shown in Fig. 3. According to the numerical results shown in Figs. 3(a1) and 3(a2), one can see that the two bound states are localized around the two bottom corners for a rectangular sample with armchair edges in the x direction and beard edges in the y direction. Interestingly, when the beard edges are modified to zigzag edges by changing only the outermost sublattices of the y-normal edges, the positions of the two bound states are found to shift dramatically to the two top corners, as illustrated in Figs. 3(b1) and 3(b2). We will adopt the edge theory to show in the next section that this is because the boundary Dirac mass has a sensitive dependence on the boundary sublattice termination, and can switch its sign when the boundary sublattice termination is changed from one type to the other.

It is worth pointing out that here the antiferromagnetic or ferrimagnetic exchange field does not favor the realization of corner bound states. This can be proven by numerical calculations or simply inferred by noting that in the limit $\lambda_v = 0$ and $\gamma = -1$, the momentum-independent

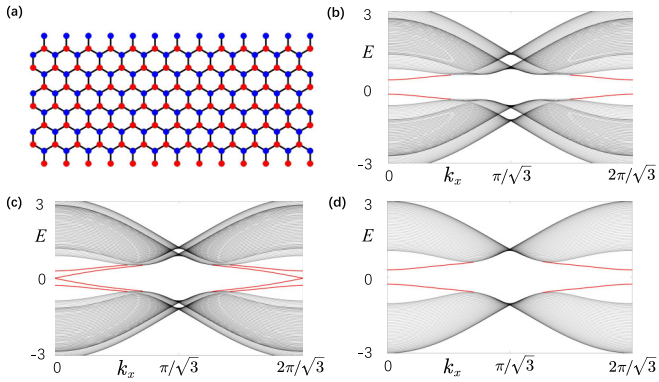

FIG. 4. Energy spectra for a ribbon with periodic boundary conditions in the x direction and beard edges in the y direction. Chosen parameters are $t = 1$, $\lambda_{so} = 0.1$, $M_x = M_y = 0.2$, $\lambda_v = 0$, and $N_y = 100$. (a) A schematic diagram of a sample with beard edges in the y direction. Blue and red sites correspond to A-type and B-type sublattices, respectively. The red-solid lines in (b)–(d) denote energy spectra of the edge states on the beard edges. (b) $\gamma = 1$, the helical edge states on the upper and lower beard edges are gapped out. (c) $\gamma = 0$, the helical edge states on the upper beard edge are gapped out, while the helical edge states on the lower beard edge remain almost gapless. (d) $\gamma = -1$, the helical edge states on the upper and lower beard edges are gapped out.

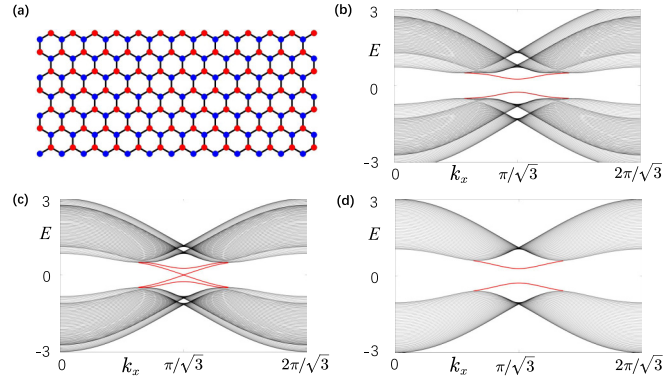

FIG. 5. Energy spectra for a ribbon with periodic boundary conditions in the x direction and zigzag edges in the y direction. Chosen parameters are $t = 1$, $\lambda_{so} = 0.1$, $M_x = M_y = 0.2$, $\lambda_v = 0$, and $N_y = 100$. (a) A schematic diagram of a sample with zigzag edges in the y direction. The red-solid lines in (b)–(d) denote energy spectra of the edge states on the zigzag edges. (b) $\gamma = 1$, the helical edge states on the upper and lower zigzag edges are gapped out. (c) $\gamma = 0$, the helical edge states on the upper zigzag edge remain almost gapless, while the helical edge states on the lower zigzag edge are gapped out. (d) $\gamma = -1$, the helical edge states on the upper and lower zigzag edges are gapped out.

antiferromagnetic exchange field anticommutes with all other terms in the Hamiltonian (2). Since this implies that the antiferromagnetic term will introduce a constant gap to the energy spectrum, which cannot be closed by tuning the parameters of all other terms, the resulting gapped phase is topologically connected to an atomic trivial insulator without any types of topological mid-gap states on the boundary.

IV. BOUND STATES AT SUBLATTICE DOMAIN WALLS

In the following, we are going to show that bound states can also be achieved even without the existence of sharp corners, and their locations can be freely tuned by taking advantage of the sublattice degrees of freedom. In a previous paper, we have revealed that for the Kane-Mele model, the boundary sublattice terminations have a strong impact on the helical edge states, such as the shift of the boundary Dirac points (the crossing point of the energy spectra for helical edge states) from one time-reversal invariant momentum to the other in the boundary Brillouin zone [59]. In addition, the sublattice terminations can also strongly affect the boundary Dirac mass induced by superconductivity and hence the formation of Dirac-mass domain walls supporting Majorana Kramers pairs [59].

To explore the impact of sublattice terminations on the boundary Dirac mass induced by exchange field, we first numerically calculate the energy spectra for a ribbon with the x direction taking periodic boundary conditions and the y direction having only beard or zigzag edges, as illustrated in Figs. 4(a) and 5(a). According to the results presented in Figs. 4(b)–4(d) and 5(b)–5(d), one can infer that the boundary energy spectra (red solid lines) for the upper and lower beard or zigzag edges are degenerate when $\gamma = \pm 1$, suggesting that the Dirac masses induced by the exchange field on the upper and lower beard or zigzag edges have the same magnitude for these two limiting cases. On the other hand, the results for $\gamma = 0$ clearly reveal that the boundary Dirac mass strongly depends on the sublattice termination for a given boundary. To be specific, let us focus on the upper y-normal boundary for a more detailed discussion. When $\gamma = 0$, based on the edges at which the mid-gap states are localized, we find that the Dirac mass is vanishingly small when the upper y-normal boundary terminates with B sublattices, as illustrated in Fig. 5(c). Obviously, the smallness of the Dirac mass should be related to the fact that exchange fields on B sublattices are absent when $\gamma = 0$. This implies that, for a given sublattice termination, the magnitude of the exchange field on the corresponding sublattices determines the main contribution to the magnitude of the Dirac mass.

As it turns out that both ferromagnetic and antiferromagnetic exchange fields can induce a finite Dirac mass to the helical edge states, regardless of the boundary sublattice terminations, a natural question to ask is: For a given type of exchange field, do the boundary Dirac masses associated with the two kinds of sublattice terminations have the same sign or opposite signs? Naively, one may think that when $\gamma > 0$, since the exchange fields take the same direction on the two types of sublattices, the Dirac masses should also take the same sign for the two kinds of sublattice terminations. In contrast, when $\gamma < 0$, since the exchange fields take opposite directions on the two kinds of sublattices, one may think that the Dirac masses associated with the two kinds of sublattice terminations should also take opposite signs. However, we find that the results are just the opposite. To show this, we focus on the upper y-normal boundary and derive the low-energy Hamiltonians describing the boundary physics on the zigzag and beard edges.

Here we focus on the limit $\lambda_v = 0$ and consider t and λ_{so} to be positive constants for the convenience of discussion. First, let us consider the upper y-normal boundary to be a beard edge [terminating with A sublattices, see the upper edge in Fig. 4(a)]. We find that the corresponding low-energy Hamiltonian has the form (see details in Appendix A)

$$\mathcal{H}_b(q_x) = vq_x s_z + M_x s_x + M_y s_y, \tag{7}$$

where q_x denotes a small momentum measured from $k_x = 0$ at which the boundary Dirac point is located (see the dispersion of edge states in Fig. 4), and the velocity of the helical edge states is $v = 3\sqrt{3}\lambda_{so}$. On the other hand, when the upper y-normal boundary is a zigzag edge [terminating with B sublattices, see the upper edge in Fig. 5(a)], we find that the low-energy Hamiltonian has the form (see details in Appendix B)

$$\mathcal{H}_z(q_x') = v' q_x' s_z + \frac{1-\gamma\eta^2}{1+\eta^2}(M_x s_x + M_y s_y), \tag{8}$$

where q_x' denotes the momentum measured from $k_x = \pi/\sqrt{3}$ at which the boundary Dirac point is located [see Fig. 5(c)], and the explicit expressions of the parameters read

$$v' = \frac{2\sqrt{3}t\lambda_{so}\eta}{1+\eta^2} + \frac{2\sqrt{3}\lambda_{so}(\eta^2-1)}{1+\eta^2},$$
$$\eta = \frac{4t\lambda_{so}}{\sqrt{t^2\left(t^2+16\lambda_{so}^2\right)} - t^2}. \tag{9}$$

In real materials, λ_{so} is commonly much smaller than t. Focusing on the regime $\lambda_{so} \ll t$, it is easy to find that $\eta \simeq t/2\lambda_{so} \gg 1$, and the Hamiltonian can be approximately reduced as

$$\mathcal{H}_z(q_x') \approx 2vq_x' s_z - \gamma(M_x s_x + M_y s_y). \tag{10}$$

The two low-energy Hamiltonians, (7) and (8), provide a clear understanding of the dependence of the boundary Dirac mass on the exchange field and sublattice termination. Remarkably, the results show that the Dirac masses on the zigzag and beard edges with the same orientation have opposite signs when $\gamma > \gamma_c = \eta^{-2}$, and the same sign when $\gamma < \gamma_c$. When $\eta \gg 1$, the critical value γ_c can be set as zero.

As Dirac masses of opposite signs lead to the formation of domain walls hosting bound states [39], apparently, the dependence of Dirac mass on the sublattice termination shown in the two low-energy boundary Hamiltonians suggests that Dirac-mass domain walls can form on the same y-normal boundary. Put it more explicitly, when $\gamma > \gamma_c$ and the y-normal boundary consists of two flat parts, with one part taking the beard edge (terminating with A sublattices) and the other taking the zigzag edge (terminating with B sublattices), then the sublattice domain walls, which correspond to the intersections of the beard and zigzag edges, are Dirac-mass domain walls hosting bound states. The numerical results shown in Fig. 6 confirm this expectation. We would like to emphasize two important properties of the sublattice domain walls that can be inferred from the numerical results. First, as the sublattice domain walls on the same boundary can support bound states, it suggests that sharp corners are not a necessary condition to achieve bound states in a second-order topological phase if the boundary Dirac mass shows sensitive dependence on the sublattice terminations. Indeed, Fig. 6 demonstrates that bound states are present even though there is no sharp corner in the system with periodic boundary conditions in one direction. Second, as the bound states are associated with the sublattice domain walls, it suggests that the locations of the bound states can be tuned by locally manipulating the sublattice termination. This fact can be intuitively inferred by a comparison of the locations of the bound states in Figs. 6(a2) and 6(b2).

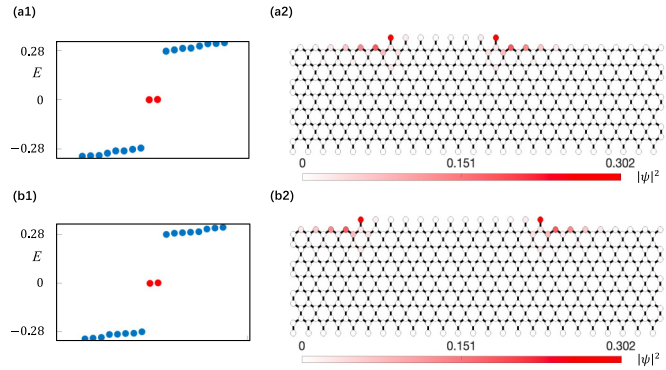

FIG. 6. Tunable bound states at the sublattice domain walls. Chosen parameters are $t = 1$, $\lambda_{so} = 0.1$, $M_x = M_y = 0.2$, $\gamma = 1$, and $\lambda_v = 0$. (a1) and (b1) show the energy spectra (only a few eigenenergies near zero energy are shown) corresponding to systems with the geometries shown in (a2) and (b2), respectively. Periodic boundary conditions are imposed in the x direction, namely, the left and right armchair edges in (a2) and (b2) are connected when diagonalizing the Hamiltonian. The red dots in (a1) and (b1) correspond to the eigenenergies of the bound states at the sublattice domain walls. The shade of the red color on the lattice sites in (a2) and (b2) reflects the weight of the probability density of the bound states.

In addition to the exchange field, it is known that the superconductivity can also induce a Dirac mass to the helical edge states and gap them out [72]. An important fact to note is that the Dirac masses induced by exchange field and superconductivity are competing in nature. Above we have shown that the Dirac masses induced by exchange field on the two sides of a sublattice domain wall can have different magnitude and signs. Apparently, this raises the possibility to realize domain walls with the Dirac mass on one side dominated by the superconductivity and on the other side dominated by the exchange field. It is known that MZMs will emerge at such domain walls [72–75]. In the following, we consider conventional s-wave superconductivity to demonstrate that MZMs can be realized at the sublattice domain walls.

V. MAJORANA ZERO MODES AT SUBLATTICE DOMAIN WALLS

Before proceeding, it is worth pointing out that a number of proposals on the realization of 2D second-order TSCs or topological superfluids have been raised in the past few years, including TI/superconductor heterostructures [22,23,75–84], superconductors with mixed-parity pairings [24,85–87], spin-orbit coupled superconductors with s + id pairing [88,89], odd-parity superconductors [25,41,90–93], etc. [94–102], also with the MZMs localized at sharp corners being the smoking gun. Among the various proposals, the TI/superconductor

heterostructures are arguably most close to implementation owing to the abundance of candidate materials.

By putting the TI described by the Kane-Mele model in proximity to an s-wave superconductor, the whole system can be effectively described by a Bogoliubov-de Gennes (BdG) Hamiltonian. Consider the basis $\Psi_{\boldsymbol{k}} = (\psi_{\boldsymbol{k}}, \psi^{\dagger}_{-\boldsymbol{k}})^T$, $H = \frac{1}{2}\sum_{\boldsymbol{k}} \Psi^{\dagger}_{\boldsymbol{k}} \mathcal{H}_{\mathrm{BdG}}(\boldsymbol{k}) \Psi_{\boldsymbol{k}}$ with

$$\mathcal{H}_{\mathrm{BdG}}(\boldsymbol{k}) = \begin{pmatrix} \mathcal{H}(\boldsymbol{k}) - \mu s_0\sigma_0 & i\Delta s_y\sigma_0 \\ -i\Delta^* s_y\sigma_0 & -\mathcal{H}^*(-\boldsymbol{k}) + \mu s_0\sigma_0 \end{pmatrix}, \quad (11)$$

where μ is the chemical potential, and Δ is the s-wave pairing amplitude. Below we will assume Δ to be a momentum-independent real constant for the convenience of discussion.

To show intuitively that MZMs can emerge at the sublattice domain walls, we derive the corresponding low-energy boundary Hamiltonian based on the BdG Hamiltonian. For generality, now we consider the staggered sublattice potential to be finite. Also focusing on the upper y-normal boundary for illustration of the key physics, we find that, for the beard edge, the low-energy boundary Hamiltonian reads (see details in Appendix A)

$$\begin{aligned} \mathcal{H}_{\mathrm{BdG;b}}(q_x) = {} & v q_x \tau_0 s_z + M_x \tau_z s_x + M_y \tau_0 s_y \\ & -(\mu - \lambda_v)\tau_z s_0 - \Delta \tau_y s_y, \end{aligned} \quad (12)$$

and for the zigzag edge, the low-energy boundary Hamiltonian reads (see details in Appendix B)

$$\begin{aligned} \mathcal{H}_{\mathrm{BdG;z}}(q'_x) = {} & v' q'_x \tau_0 s_z + \frac{1-\gamma\eta^2}{1+\eta^2}(M_x \tau_z s_x + M_y \tau_0 s_y) \\ & -\left(\mu + \frac{\eta^2 - 1}{1+\eta^2}\lambda_v\right)\tau_z s_0 - \Delta \tau_y s_y, \end{aligned} \quad (13)$$

where τ_0 and $\tau_{x,y,z}$ are identity matrix and Pauli matrices in the particle-hole space. It is readily seen that the staggered potential effectively induces an opposite shift in the chemical potential. This is easy to understand since the terminating sublattices for these two kinds of edges are different and hence have different potentials. As will be shown below, this can benefit the realization of MZMs at the sublattice domain walls.

Without loss of generality, let us still focus on the regime $t \gg \lambda_{\mathrm{so}}$ so that $\eta \gg 1$ and the form of the low-energy boundary Hamiltonian on the zigzag edge can be simplified as

$$\begin{aligned} \mathcal{H}_{\mathrm{BdG;z}}(q'_x) \approx {} & v' q'_x \tau_0 s_z - \gamma(M_x \tau_z s_x + M_y \tau_0 s_y) \\ & -(\mu + \lambda_v)\tau_z s_0 - \Delta \tau_y s_y. \end{aligned} \quad (14)$$

It is straightforward to find that the gap-closing condition of the boundary energy spectrum for the beard edge is

$$M = \sqrt{(\mu - \lambda_v)^2 + \Delta^2}, \quad (15)$$

and for the zigzag edge, the gap-closing condition is

$$|\gamma| M = \sqrt{(\mu + \lambda_v)^2 + \Delta^2}, \quad (16)$$

where $M = \sqrt{M_x^2 + M_y^2}$. It is worth noting that, for simplicity, the gap-closing condition for the zigzag edge is obtained via the approximate Hamiltonian (14). The accurate condition can also be easily obtained according to the Hamiltonian (13), but will have a somewhat more complex expression [see Eq. (B15)]. In Fig. 7, we assume that the exchange field is fixed, and show the evolution of the boundary energy spectra (red solid lines) with respect to μ. We find that the critical μ_c at which the boundary energy gap on the upper edge gets closed agrees excellently with the value predicted by the low-energy boundary Hamiltonians (12) and (13), reflecting the power of the edge theory in describing the boundary physics.

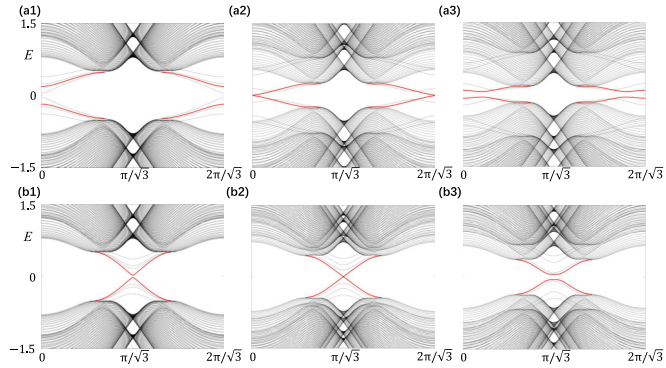

FIG. 7. The evolution of boundary energy gap on the upper y-normal edge with respect to μ for a cylindrical geometry with periodic boundary conditions in the x direction. Chosen parameters are $t = 1$, $\lambda_{\mathrm{so}} = 0.1$, $M_x = M_y = 0.2$, $\gamma = 0.5$, $\lambda_v = 0$, and $\Delta = 0.1$. For (a1)–(a3), the open boundaries are beard edges, and the critical value of μ at which the boundary energy gap of the upper edge is equal to 0.265 according to the chosen parameters. For (b1)–(b3), the open boundaries are zigzag edges, and the critical value of μ is equal to 0.077. (a1) $\mu = 0$, (a2) $\mu = 0.265$, (a3) $\mu = 0.35$, (b1) $\mu = 0$, (b2) $\mu = 0.07$, and (b3) $\mu = 0.15$.

For a given edge, the gap closure of the boundary energy spectrum signals a change of the boundary topology. For the upper beard edge, its Dirac mass falls into the superconductivity-dominated region when $M < M_{c,b} \equiv \sqrt{(\mu - \lambda_v)^2 + \Delta^2}$, and the exchange-field-dominated region when $M > M_{c,b}$. Similarly, the Dirac mass of the upper zigzag edge falls into the superconductivity-dominated region when $|\gamma| M < M_{c,z} \equiv \sqrt{(\mu + \lambda_v)^2 + \Delta^2}$, and the exchange-field-dominated region when $|\gamma| M > M_{c,z}$. When the Dirac masses on the upper beard and zigzag edges fall into different regions, the sublattice domain walls will bind MZMs.

Without loss of generality, let us consider $\mu \geqslant 0$ and $\lambda_v \geqslant 0$ to exemplify the physics. With this choice, the condition to realize MZMs at the sublattice domain walls is

$$M > M_{c,b}, \quad |\gamma| M < M_{c,z}. \quad (17)$$

Since the two inequalities above are independent of the sign of γ, it indicates that MZMs at sublattice domain walls can be achieved for both ferromagnetic and antiferromagnetic exchange fields as long as the two inequalities are simultaneously fulfilled.

We would like to make a further remark on Eq. (17). The two inequalities suggest that the topological region supporting MZMs can be made very sizable. For instance, by tuning $\mu = \lambda_v$, $\gamma = 0$, MZMs can be realized once $M > |\Delta|$. In Fig. 8, we consider a ferromagnetic exchange field and show the realization of MZMs at the sublattice domain walls for a sample with cylindrical geometry (left and right edges are connected, hence there is no sharp corner). By a comparison of Figs. 8(a2)

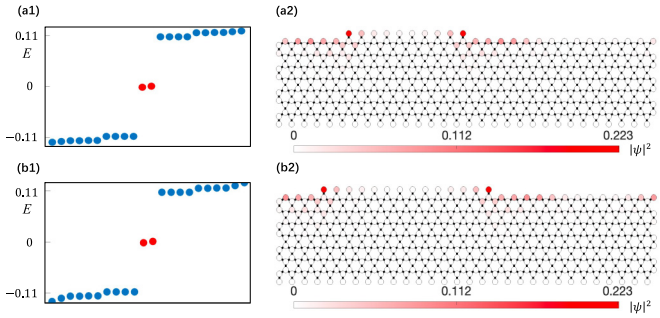

FIG. 8. Tunable MZMs at sublattice domain walls for a ferromagnetic exchange field. Chosen parameters are $t = 1$, $\lambda_{so} = 0.1$, $M_x = M_y = 0.2$, $\gamma = 1$, $\Delta = 0.15$, $\lambda_v = 0.2$, and $\mu = 0.2$. The geometry considered is depicted in (a2) and (b2), and a few corresponding eigenenergies near zero energy are shown in (a1) and (b1). Periodic boundary conditions are imposed in the x direction. The red dots in the energy spectra denote MZMs (their energies are not exactly zero due to splitting induced by finite-size effects) at the sublattice domain walls. The right panels show their probability density profiles with the shade of the red color on the lattice sites reflecting the weight.

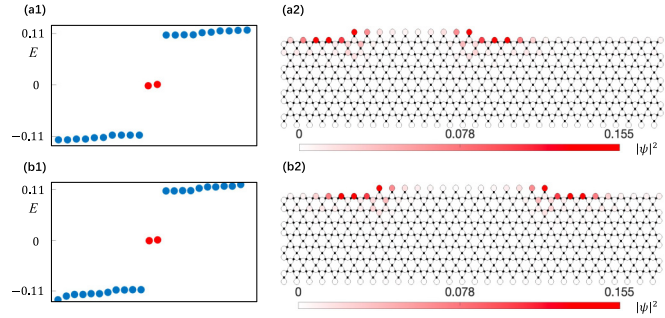

FIG. 9. Tunable MZMs at sublattice domain walls for an antiferromagnetic exchange field. All parameters are the same as in Fig. 8 except $\gamma = -1$.

and 8(b2), it is easy to see that the positions of MZMs can be tuned to any place on the upper edge by manipulating the boundary sublattice terminations. Apparently, one can also manipulate two sublattice domain walls to move toward each other, then one can study the splitting and annihilation of two MZMs. In Fig. 9, we consider an antiferromagnetic exchange field and show explicitly that the physics is similar.

VI. DISCUSSION AND CONCLUSIONS

In this paper, we have shown when the lattice structure has sublattice degrees of freedom, the bound states in second-order TIs and TSCs are unnecessarily pinned at some specific sharp corners. By adjusting the boundary sublattice terminations to form sublattice domain walls, we have shown that the positions of the bound states can be freely manipulated. For the honeycomb lattice considered, if one designs a sample with the diamond shape as considered in Ref. [36] or also with the honeycomb shape so that all edges take either the beard-type or the zigzag-type sublattice termination, then the sublattice domain walls allow to form at any place on the boundary. Accordingly, the positions of the bound states can be manipulated to any place on the boundary. It is reasonable to expect that such a sublattice-enriched tunability would benefit the manipulation and application of the bound states, e.g., braiding MZMs [103–105].

About the experimental implementation, we would like to first emphasize that our predictions are relevant to both quantum materials and classical systems. For quantum-material realization, one route is to apply a magnetic field to a two-dimensional first-order TI described by the Kane-Mele model, such as silicene, germanene, stanene [106–108]. As twisted transition metal dichalcogenide homobilayers are predicted to effectively realize Kane-Mele model and allow various types of magnetic orders [109,110], they may also serve as a platform to explore the predicted boundary physics. Another route is to find intrinsic magnetic second-order TI with sublattice degrees of freedom through first-principle calculations [37,111,112]. Generalizations to the superconducting counterpart can be simply achieved by putting the above two classes of systems in proximity to a superconductor [73,75], as demonstrated in Sec. V. In quantum materials, as the lattice constant is at the atomic length scale, adjusting boundary sublattice terminations requires sophisticated tools, e.g., scanning tunneling microscope or scanning force microscope [113,114]. For classical-system realization, since the Kane-Mele model subjected to an in-plane Zeeman field has been effectively realized in an acoustic system [38], our prediction on the realization of bound states at sublattice domain walls in a second-order TI can be immediately explored. It is worth emphasizing that the manipulation of bound states at sublattice domain walls is expected to be much easier in classical systems than in quantum materials due to their much larger length scales. For instance, one can simply remove one sublattice on the boundary in an electric circuit by just removing all wires connected to that sublattice. As a final remark, it is worth pointing out that, since the wave functions of the helical edge states decay exponentially away from the boundary, the boundary Dirac masses are mainly contributed by the exchange field and superconductivity at the neighborhood of the edges. In other words, the predicted boundary physics in this paper can also be realized even when the exchange field and superconductivity are nonuniform or only appear at the neighborhood of the edges.

In summary, we have shown that the sublattice degrees of freedom and second-order topology have an interesting interplay, which can lead to the presence of rich boundary physics, such as the formation of highly controllable bound states.

ACKNOWLEDGMENTS

D.Z. and Z.Y. are supported by the National Natural Science Foundation of China (Grants No.11904417 and No. 12174455) and the Natural Science Foundation of Guangdong Province (Grant No. 2021B1515020026). M.Kh. is supported by the NSERC of Canada.

APPENDIX A: LOW-ENERGY BOUNDARY HAMILTONIAN ON THE BEARD EDGE

The low-energy boundary Hamiltonians on the beard and zigzag edges for the Kane-Mele model have been derived in

a previous paper of ours [59], but there we did not consider the staggered potential and exchange field. Here for self-consistency, we provide the main steps of the derivation.

Start with the BdG Hamiltonian in the momentum space,

$$\begin{aligned}\mathcal{H}_{\mathrm{BdG}}(\boldsymbol{k}) = & t\left(2\cos\frac{\sqrt{3}k_x}{2}\cos\frac{k_y}{2}+\cos k_y\right)\tau_z s_0\sigma_x \\ & -t\left(2\cos\frac{\sqrt{3}k_x}{2}\sin\frac{k_y}{2}-\sin k_y\right)\tau_z s_0\sigma_y \\ & +2\lambda_{\mathrm{so}}\left(\sin\sqrt{3}k_x-2\sin\frac{\sqrt{3}k_x}{2}\cos\frac{3k_y}{2}\right)\tau_0 s_z\sigma_z \\ & +\lambda_v\tau_z s_0\sigma_z-\mu\tau_z s_0\sigma_0+\frac{1+\gamma}{2}(M_x\tau_z s_x \\ & +M_y\tau_0 s_y)\sigma_0+\frac{1-\gamma}{2}(M_x\tau_z s_x+M_y\tau_0 s_y)\sigma_z \\ & -\Delta\tau_y s_y\sigma_0, \end{aligned} \tag{A1}$$

where τ_i, s_i, and σ_i are Pauli matrices acting on the particle-hole, spin and sublattice degrees of freedom, respectively, and τ_0, s_0, and σ_0 denote identity matrices in the respective subspaces. For notational simplicity, the nearest-neighbor lattice constant has been set to unity.

When the upper boundary is a beard edge, the numerical results show that the corresponding boundary Dirac point is located at the time-reversal invariant momentum $k_x = 0$ in the reduced boundary Brillouin zone. To derive the low-energy boundary Hamiltonian in an analytical way, we expand the bulk Hamiltonian around $k_x = 0$ up to the linear order in momentum (the expansion is only performed in the k_x direction), leading to

$$\begin{aligned}\mathcal{H}_{\mathrm{BdG}}(q_x,k_y) = & t\left(2\cos\frac{k_y}{2}+\cos k_y\right)\tau_z s_0\sigma_x \\ & -t\left(2\sin\frac{k_y}{2}-\sin k_y\right)\tau_z s_0\sigma_y \\ & +2\sqrt{3}\lambda_{\mathrm{so}}q_x\left(1-\cos\frac{3k_y}{2}\right)\tau_0 s_z\sigma_z \\ & +\lambda_v\tau_z s_0\sigma_z-\mu\tau_z s_0\sigma_0+\frac{1+\gamma}{2}(M_x\tau_z s_x \\ & +M_y\tau_0 s_y)\sigma_0+\frac{1-\gamma}{2}(M_x\tau_z s_x+M_y\tau_0 s_y)\sigma_z \\ & -\Delta\tau_y s_y\sigma_0, \end{aligned} \tag{A2}$$

where q_x denotes a small momentum, which is measured from $k_x = 0$. In the next step, we decompose the Hamiltonian into two parts, $\mathcal{H}_{\mathrm{BdG}} = \mathcal{H}_0 + \mathcal{H}_1$, with

$$\begin{aligned}\mathcal{H}_0(q_x,k_y) = & t\left(2\cos\frac{k_y}{2}+\cos k_y\right)\tau_z s_0\sigma_x \\ & -t\left(2\sin\frac{k_y}{2}-\sin k_y\right)\tau_z s_0\sigma_y, \\ \mathcal{H}_1(q_x,k_y) = & 2\sqrt{3}\lambda_{so}q_x\left(1-\cos\frac{3k_y}{2}\right)\tau_0 s_z\sigma_z+\lambda_v\tau_z s_0\sigma_z \\ & -\mu\tau_z s_0\sigma_0+\frac{1+\gamma}{2}(M_x\tau_z s_x+M_y\tau_0 s_y)\sigma_0 \\ & +\frac{1-\gamma}{2}(M_x\tau_z s_x+M_y\tau_0 s_y)\sigma_z-\Delta\tau_y s_y\sigma_0. \end{aligned} \tag{A3}$$

We will treat $\mathcal{H}_1$ as a perturbation, which is justified at least when the parameters in $\mathcal{H}_1$ are all much smaller than t. One can see that the two terms in $\mathcal{H}_0$ have a momentum dependence similar to the Su-Schrieffer-Heeger (SSH) model [115], but with the dimension of the Hamiltonian being increased from 2 to 8. On the other hand, $\mathcal{H}_0$ is independent of q_x. This implies that each y-normal edge may harbor a zero-energy flat band with fourfold degeneracy if periodic boundary conditions are imposed in the x direction. To confirm this, we focus on the upper y-normal edge for illustration.

To simplify the derivation, we consider a half-infinity sample with the boundary corresponding to the upper beard edge. Accordingly, a natural basis is $\Psi_{q_x} = (c_{1,A,q_x}, c_{1,B,q_x}, c_{2,A,q_x}, c_{2,B,q_x}, ..., c_{n,A,q_x}, c_{n,B,q_x}, ...)^T$ with $c_{n,\alpha,q_x} = (c_{n,\alpha,q_x,\uparrow}, c_{n,\alpha,q_x,\downarrow}, c^\dagger_{n,\alpha,-q_x,\uparrow}, c^\dagger_{n,\alpha,-q_x,\downarrow})$, where $\alpha = \{A, B\}$. Under this basis, the matrix form of $\mathcal{H}_0$ reads

$$\mathcal{H}_0 = \begin{pmatrix} 0 & t\tau_z s_0 & 0 & 0 & 0 & \cdots \\ t\tau_z s_0 & 0 & 2t\tau_z s_0 & 0 & 0 & \cdots \\ 0 & 2t\tau_z s_0 & 0 & t\tau_z s_0 & 0 & \cdots \\ 0 & 0 & t\tau_z s_0 & 0 & 2t\tau_z s_0 & \cdots \\ 0 & 0 & 0 & 2t\tau_z s_0 & 0 & \cdots \\ \vdots & \vdots & \vdots & \vdots & \vdots & \ddots \end{pmatrix}. \tag{A4}$$

Here each "0" element denotes a four-by-four null matrix. The wave functions of the zero-energy bound states are determined by solving the eigenvalue equation $\mathcal{H}_0|\Psi_\alpha\rangle = 0$. By observation, one can notice that τ_z and s_z both commute with $\mathcal{H}_0$, so $|\Psi_\alpha\rangle$ can be assigned with the form

$$|\Psi_{\tau s}\rangle = (\psi_{1A}, \psi_{1B}, \psi_{2A}, \psi_{2B}, ...)^T \otimes |\tau_z = \tau\rangle \otimes |s_z = s\rangle, \tag{A5}$$

where $|\tau_z = \tau\rangle$ and $|s_z = s\rangle$ with $\tau = \pm 1$ and $s = \pm 1$ correspond to the two eigenstates of τ_z and s_z, respectively. Solving the eigenvalue equation $\mathcal{H}_0|\Psi_{\tau s}\rangle = 0$ is equivalent to solving the following iterative equations:

$$\begin{aligned} t\psi_{1B} &= 0, \\ t\psi_{1A}+2t\psi_{2A} &= 0, \\ 2t\psi_{1B}+t\psi_{2B} &= 0, \\ &\cdots \\ t\psi_{nA}+2t\psi_{(n+1)A} &= 0, \\ 2t\psi_{nB}+t\psi_{(n+1)B} &= 0, \\ &\cdots. \end{aligned} \tag{A6}$$

According to the iterative structure, it is easy to find

$$\psi_{(n+1)A} = -\tfrac{1}{2}\psi_{nA}, \quad \psi_{nB} = 0. \tag{A7}$$

Therefore, the eigenvectors take the form

$$\begin{aligned}|\Psi_{\tau s}\rangle = & \mathcal{N}\left(1, 0, -\tfrac{1}{2}, 0, \cdots, \left(-\tfrac{1}{2}\right)^{(n-1)}, 0, \cdots\right)^T \\ & \otimes|\tau_z = \tau\rangle \otimes |s_z = s\rangle, \end{aligned} \tag{A8}$$

where $\mathcal{N}$ denotes the normalization constant. According to the normalization condition $\langle\Psi_{\tau s}|\Psi_{\tau s}\rangle = 1$, simple calculations reveal

$$\mathcal{N}^2\sum_{n=0}^{\infty}\frac{1}{2^{2n}} = \mathcal{N}^2\frac{1}{1-\frac{1}{4}} = \frac{4}{3}\mathcal{N}^2 = 1, \tag{A9}$$

so $\mathcal{N} = \frac{\sqrt{3}}{2}$. As ψ_{nA} decays exponentially with the increase of n, the existence of four such eigenvectors indicates the existence of four zero-energy bound states, confirming the correctness of the simple analysis based on the connection to SSH model. It is worth noting that the TI has only one pair of gapless helical states on a given edge, so there should exist only two degenerate zero-energy bound states at $q_x = 0$. Here the existence of four zero-energy bound states originates from the doubling due to the introduction of particle-hole redundancy. The low-energy Hamiltonian on the upper y-normal beard edge is then obtained by projecting $\mathcal{H}_1$ onto the four-dimensional subspace spanned by the four orthogonal eigenstates. Put it explicitly, the matrix elements of the low-energy boundary Hamiltonian are given by

$$[\mathcal{H}_{\mathrm{BdG,b}}(q_x)]_{\tau s,\tau' s'} = \langle\Psi_{\tau s}|\mathcal{H}_1(q_x)|\Psi_{\tau' s'}\rangle. \tag{A10}$$

It is worth noting that here $\mathcal{H}_1(q_x)$ is also an infinitely large matrix, and its form is given by a partial Fourier transform of $\mathcal{H}_1(q_x, k_y)$ in the y direction. By some straightforward calculations and choosing $(|\Psi_{11}\rangle, |\Psi_{1-1}\rangle, |\Psi_{-11}\rangle, |\Psi_{-1-1}\rangle)^T$ as the basis for the low-energy boundary Hamiltonian, one can obtain (more details on how to determine each term in the low-energy Hamiltonian can be found in Ref. [59])

$$\begin{aligned}\mathcal{H}_{\mathrm{BdG,b}}(q_x) = {} & vq_x\tau_0 s_z + M_x\tau_z s_x + M_y\tau_0 s_y \\ & -(\mu-\lambda_v)\tau_z s_0 - \Delta\tau_y s_y,\end{aligned} \tag{A11}$$

where $v = 3\sqrt{3}\lambda_{\mathrm{so}}$. Without the superconductivity (the particle-hole redundancy is accordingly removed) and staggered potential, the low-energy boundary Hamiltonian reduces to the form in Eq. (7). The boundary energy spectra associated with this boundary Hamiltonian read

$$E(q_x) = \pm\sqrt{F \pm 2\sqrt{G}}, \tag{A12}$$

where $F = v^2q_x^2 + M^2 + (\mu-\lambda_v)^2 + \Delta^2$ and $G = (\mu-\lambda_v)^2(v^2q_x^2 + M^2) + M^2\Delta^2$. The gap of the boundary energy spectra gets closed at $q_x = 0$ when the following condition is fulfilled,

$$M = \sqrt{(\mu-\lambda_v)^2 + \Delta^2}. \tag{A13}$$

APPENDIX B: LOW-ENERGY BOUNDARY HAMILTONIAN ON THE ZIGZAG EDGE

Following the same spirit, we can derive the low-energy boundary Hamiltonian on the upper y-normal zigzag edge. Since numerical results show that the boundary Dirac point on the y-normal zigzag edge is located at $k_x = \pi/\sqrt{3}$, we similarly expand the Hamiltonian up to the linear order in momentum, which then gives

$$\begin{aligned}\mathcal{H}_{\mathrm{BdG}}(q_x', k_y) = {} & t\left(-\sqrt{3}q_x'\cos\frac{k_y}{2} + \cos k_y\right)\tau_z s_0\sigma_x \\ & + t\left(\sqrt{3}q_x'\sin\frac{k_y}{2} + \sin k_y\right)\tau_z s_0\sigma_y \\ & + 2\lambda_{\mathrm{so}}\left(-\sqrt{3}q_x' - 2\cos\frac{3k_y}{2}\right)\tau_0 s_z\sigma_z \\ & + \lambda_v\tau_z s_0\sigma_z - \mu\tau_z s_0\sigma_0 + \frac{1+\gamma}{2}(M_x\tau_z s_x \\ & + M_y\tau_0 s_y)\sigma_0 + \frac{1-\gamma}{2}(M_x\tau_z s_x + M_y\tau_0 s_y)\sigma_z \\ & - \Delta\tau_y s_y\sigma_0,\end{aligned} \tag{B1}$$

where q_x' denotes a small momentum measured from $k_x = \pi/\sqrt{3}$. Similarly, we decompose the Hamiltonian into two parts, $\mathcal{H} = \mathcal{H}_0 + \mathcal{H}_1$, with

$$\begin{aligned}\mathcal{H}_0(q_x', k_y) = {} & t\cos k_y\tau_z s_0\sigma_x + t\sin k_y\tau_z s_0\sigma_y \\ & - 4\lambda_{\mathrm{so}}\cos\frac{3k_y}{2}\tau_0 s_z\sigma_z,\end{aligned}$$

$$\begin{aligned}\mathcal{H}_1(q_x', k_y) = {} & -\sqrt{3}tq_x'\cos\frac{k_y}{2}\tau_z s_0\sigma_x + \sqrt{3}tq_x'\sin\frac{k_y}{2}\tau_z s_0\sigma_y \\ & - 2\sqrt{3}\lambda_{\mathrm{so}}q_x'\tau_0 s_z\sigma_z + \lambda_v\tau_z s_0\sigma_z - \mu\tau_z s_0\sigma_0 \\ & + \frac{1+\gamma}{2}(M_x\tau_z s_x + M_y\tau_0 s_y)\sigma_0 + \frac{1-\gamma}{2}(M_x\tau_z s_x \\ & + M_y\tau_0 s_y)\sigma_z - \Delta\tau_y s_y\sigma_0.\end{aligned} \tag{B2}$$

Also focusing on the upper y-normal boundary, the change from a beard edge to a zigzag edge is accompanied with the change of terminating sublattice from sublattice A to sublattice B. For simplicity, we also consider the half-infinity geometry, and then the corresponding basis becomes $\Psi_{q_x'} = (c_{1,B,q_x'}, c_{2,A,q_x'}, c_{2,B,q_x'}, c_{3,A,q_x'}, c_{3,B,q_x'}, \ldots)^T$. Under this basis, the corresponding matrix form of $\mathcal{H}_0$ reads

$$\mathcal{H}_0 = \begin{pmatrix} 0 & T_1 & 0 & 0 & 0 & \cdots \\ T_1^\dagger & 0 & T_1 & 0 & 0 & \cdots \\ 0 & T_1^\dagger & 0 & T_1 & 0 & \cdots \\ 0 & 0 & T_1^\dagger & 0 & T_1 & \cdots \\ 0 & 0 & 0 & T_1^\dagger & 0 & \cdots \\ \vdots & \vdots & \vdots & \vdots & \vdots & \ddots \end{pmatrix}, \tag{B3}$$

where now each "0" element in $\mathcal{H}_0$ is an eight-by-eight null matrix, and

$$T_1 = \begin{pmatrix} 2\lambda_{\mathrm{so}}\tau_0 s_z & 0 \\ t\tau_z s_0 & -2\lambda_{\mathrm{so}}\tau_0 s_z \end{pmatrix}. \tag{B4}$$

As here τ_z and s_z also commute with $\mathcal{H}_0$, the wave functions for zero-energy bound states can also be assigned with the from

$$\begin{aligned}|\Psi_{\tau s}\rangle = {} & (\psi_{1B}, \psi_{2A}, \psi_{2B}, \psi_{3A}, \psi_{3B}, \ldots)^T \\ & \otimes|\tau_z = \tau\rangle \otimes |s_z = s\rangle.\end{aligned} \tag{B5}$$

The eigenvalue equation $\mathcal{H}_0|\Psi_{\tau s}\rangle = 0$ leads to the following iterative equations:

$$\begin{aligned} 2\lambda_{\mathrm{so,s}}\psi_{2B} &= 0, \\ t_\tau\psi_{2B} - 2\lambda_{\mathrm{so,s}}\psi_{3A} &= 0, \\ 2\lambda_{\mathrm{so,s}}\psi_{1B} + t_\tau\psi_{2A} + 2\lambda_{\mathrm{so,s}}\psi_{3B} &= 0, \\ -2\lambda_{\mathrm{so,s}}\psi_{2A} + t_\tau\psi_{3B} - 2\lambda_{\mathrm{so,s}}\psi_{4A} &= 0, \\ &\cdots \\ 2\lambda_{\mathrm{so,s}}\psi_{(n-1)B} + t_\tau\psi_{nA} + 2\lambda_{\mathrm{so,s}}\psi_{(n+1)B} &= 0, \\ -2\lambda_{\mathrm{so,s}}\psi_{nA} + t_\tau\psi_{(n+1)B} - 2\lambda_{\mathrm{so,s}}\psi_{(n+2)A} &= 0, \\ &\cdots, \end{aligned} \tag{B6}$$

where $t_\tau = t\tau$ and $\lambda_{\mathrm{so,s}} = \lambda_{\mathrm{so}}s$. The solutions are found to take the form (more details can be found in Ref. [59])

$$\begin{aligned} |\Psi_{\tau s}\rangle = \mathcal{N}(&\eta_{\tau s}, 1, 0, 0, \xi\eta_{\tau s}, \xi, 0, 0, \xi^2\eta_{\tau s}, \xi^2, \ldots)^T \\ &\otimes|\tau_z = \tau\rangle \otimes |s_z = s\rangle, \end{aligned} \tag{B7}$$

where

$$\begin{aligned} \xi &= \frac{\sqrt{t^2\left(t^2+16\lambda_{\mathrm{so}}^2\right)} - \left(t^2+8\lambda_{\mathrm{so}}^2\right)}{8\lambda_{\mathrm{so}}^2}, \\ \mathcal{N} &= \sqrt{\frac{1-\xi^2}{1+\eta^2}}, \\ \eta &= \frac{4t\lambda_{\mathrm{so}}}{\sqrt{t^2\left(t^2+16\lambda_{\mathrm{so}}^2\right)} - t^2}, \end{aligned} \tag{B8}$$

and $\eta_{\tau s} = -\tau s\eta$. Similarly, projecting $\mathcal{H}_1$ onto the four-dimensional subspace spanned by the four orthogonal wave functions associated with the four zero-energy bound states, one can obtain the low-energy boundary Hamiltonian, which reads

$$\begin{aligned} \mathcal{H}_{\mathrm{BdG;z}}(q_x') = v'q_x'\tau_0 s_z + \frac{1-\gamma\eta^2}{1+\eta^2}(M_x\tau_z s_x + M_y\tau_0 s_y) \\ -\left(\mu + \frac{\eta^2-1}{1+\eta^2}\lambda_v\right)\tau_z s_0 - \Delta\tau_y s_y, \end{aligned} \tag{B9}$$

where

$$v' = \frac{2\sqrt{3}t\eta + 2\sqrt{3}\lambda_{so}(\eta^2-1)}{1+\eta^2}. \tag{B10}$$

For real materials, it is common that $t \gg \lambda_{\mathrm{so}}$. When $t \gg \lambda_{\mathrm{so}}$, one finds

$$\begin{aligned} \eta &= \frac{4t\lambda_{\mathrm{so}}}{\sqrt{t^2\left(t^2+16\lambda_{\mathrm{so}}^2\right)} - t^2} \\ &\approx \frac{4t\lambda_{\mathrm{so}}}{\left(t^2+8\lambda_{\mathrm{so}}^2\right) - t^2} \\ &= \frac{t}{2\lambda_{\mathrm{so}}} \gg 1. \end{aligned} \tag{B11}$$

In this limit, $v' \approx 2v$, and the boundary Hamiltonian for the zigzag edge can be simplified as

$$\begin{aligned} \mathcal{H}_{\mathrm{BdG;z}}(q_x') \approx v'q_x'\tau_0 s_z - \gamma(M_x\tau_z s_x + M_y\tau_0 s_y) \\ -(\mu+\lambda_v)\tau_z s_0 - \Delta\tau_y s_y. \end{aligned} \tag{B12}$$

The corresponding boundary energy spectra read

$$E(q_x') = \pm\sqrt{F' \pm 2\sqrt{G'}}, \tag{B13}$$

where $F' = v'^2q_x^2 + \gamma^2M^2 + (\mu+\lambda_v)^2 + \Delta^2$ and $G' = (\mu+\lambda_v)^2(v'^2q_x^2 + \gamma^2M^2) + \gamma^2M^2\Delta^2$. The gap of the boundary energy spectra gets closed at $q_x' = 0$ when the following condition is fulfilled,

$$|\gamma|M = \sqrt{(\mu+\lambda_v)^2 + \Delta^2}. \tag{B14}$$

If one determines the gap-closing condition according to the Hamiltonian (B9), one only needs to do the replacement, $\gamma \to (1-\gamma\eta^2)/(1+\eta^2)$, and $\lambda_v \to \lambda_v(\eta^2-1)/(1+\eta^2)$, namely, the criterion (B14) for gap closure is simply modified as

$$\left|\frac{1-\gamma\eta^2}{1+\eta^2}\right|M = \sqrt{\left(\mu + \frac{\eta^2-1}{1+\eta^2}\lambda_v\right)^2 + \Delta^2}. \tag{B15}$$

[1] C. L. Kane and E. J. Mele, Quantum Spin Hall Effect in Graphene, Phys. Rev. Lett. **95**, 226801 (2005).

[2] C. L. Kane and E. J. Mele, Z_2 Topological Order and the Quantum Spin Hall Effect, Phys. Rev. Lett. **95**, 146802 (2005).

[3] B. A. Bernevig and S.-C. Zhang, Quantum Spin Hall Effect, Phys. Rev. Lett. **96**, 106802 (2006).

[4] B. A. Bernevig, T. L. Hughes, and S.-C. Zhang, Quantum spin Hall effect and topological phase transition in HgTe quantum wells, Science **314**, 1757 (2006).

[5] M. König, S. Wiedmann, C. Brüne, A. Roth, H. Buhmann, L. W. Molenkamp, X.-L. Qi, and S.-C. Zhang, Quantum spin Hall insulator state in HgTe quantum wells, Science **318**, 766 (2007).

[6] M. Z. Hasan and C. L. Kane, *Colloquium*: Topological insulators, Rev. Mod. Phys. **82**, 3045 (2010).

[7] X.-L. Qi and S.-C. Zhang, Topological insulators and superconductors, Rev. Mod. Phys. **83**, 1057 (2011).

[8] T. Ozawa, H. M. Price, A. Amo, N. Goldman, M. Hafezi, L. Lu, M. C. Rechtsman, D. Schuster, J. Simon, O. Zilberberg, and I. Carusotto, Topological photonics, Rev. Mod. Phys. **91**, 015006 (2019).

[9] G. Ma, M. Xiao, and C. T. Chan, Topological phases in acoustic and mechanical systems, Nat. Rev. Phys. **1**, 281 (2019).

[10] C.-K. Chiu, J. C. Y. Teo, A. P. Schnyder, and S. Ryu, Classification of topological quantum matter with symmetries, Rev. Mod. Phys. **88**, 035005 (2016).

[11] M. Sitte, A. Rosch, E. Altman, and L. Fritz, Topological Insulators in Magnetic Fields: Quantum Hall Effect and Edge Channels with a Nonquantized θ Term, Phys. Rev. Lett. **108**, 126807 (2012).

[12] F. Zhang, C. L. Kane, and E. J. Mele, Surface State Magnetization and Chiral Edge States on Topological Insulators, Phys. Rev. Lett. **110**, 046404 (2013).

[13] W. A. Benalcazar, B. A. Bernevig, and T. L. Hughes, Quantized electric multipole insulators, Science **357**, 61 (2017).

[14] W. A. Benalcazar, B. A. Bernevig, and T. L. Hughes, Electric multipole moments, topological multipole moment pumping, and chiral hinge states in crystalline insulators, Phys. Rev. B **96**, 245115 (2017).

[15] F. Schindler, A. M. Cook, M. G. Vergniory, Z. Wang, S. S. P. Parkin, B. A. Bernevig, and T. Neupert, Higher-order topological insulators, Sci. Adv. **4**, eaat0346 (2018).

[16] Z. Song, Z. Fang, and C. Fang, $(d-2)$-Dimensional Edge States of Rotation Symmetry Protected Topological States, Phys. Rev. Lett. **119**, 246402 (2017).

[17] J. Langbehn, Y. Peng, L. Trifunovic, F. von Oppen, and P. W. Brouwer, Reflection-Symmetric Second-Order Topological Insulators and Superconductors, Phys. Rev. Lett. **119**, 246401 (2017).

[18] F. Liu and K. Wakabayashi, Novel Topological Phase with a Zero Berry Curvature, Phys. Rev. Lett. **118**, 076803 (2017).

[19] M. Ezawa, Higher-Order Topological Insulators and Semimetals on the Breathing Kagome and Pyrochlore Lattices, Phys. Rev. Lett. **120**, 026801 (2018).

[20] M. Geier, L. Trifunovic, M. Hoskam, and P. W. Brouwer, Second-order topological insulators and superconductors with an order-two crystalline symmetry, Phys. Rev. B **97**, 205135 (2018).

[21] E. Khalaf, Higher-order topological insulators and superconductors protected by inversion symmetry, Phys. Rev. B **97**, 205136 (2018).

[22] Z. Yan, F. Song, and Z. Wang, Majorana Corner Modes in a High-Temperature Platform, Phys. Rev. Lett. **121**, 096803 (2018).

[23] Q. Wang, C.-C. Liu, Y.-M. Lu, and F. Zhang, High-Temperature Majorana Corner States, Phys. Rev. Lett. **121**, 186801 (2018).

[24] Y. Wang, M. Lin, and T. L. Hughes, Weak-pairing higher order topological superconductors, Phys. Rev. B **98**, 165144 (2018).

[25] Z. Yan, Higher-Order Topological Odd-Parity Superconductors, Phys. Rev. Lett. **123**, 177001 (2019).

[26] T. Liu, Y.-R. Zhang, Q. Ai, Z. Gong, K. Kawabata, M. Ueda, and F. Nori, Second-Order Topological Phases in Non-Hermitian Systems, Phys. Rev. Lett. **122**, 076801 (2019).

[27] K. Kudo, T. Yoshida, and Y. Hatsugai, Higher-Order Topological Mott Insulators, Phys. Rev. Lett. **123**, 196402 (2019).

[28] R. Chen, C.-Z. Chen, J.-H. Gao, B. Zhou, and D.-H. Xu, Higher-Order Topological Insulators in Quasicrystals, Phys. Rev. Lett. **124**, 036803 (2020).

[29] B. Huang and W. V. Liu, Floquet Higher-Order Topological Insulators with Anomalous Dynamical Polarization, Phys. Rev. Lett. **124**, 216601 (2020).

[30] H. Hu, B. Huang, E. Zhao, and W. V. Liu, Dynamical Singularities of Floquet Higher-Order Topological Insulators, Phys. Rev. Lett. **124**, 057001 (2020).

[31] W. Zhang, D. Zou, Q. Pei, W. He, J. Bao, H. Sun, and X. Zhang, Experimental Observation of Higher-Order Topological Anderson Insulators, Phys. Rev. Lett. **126**, 146802 (2021).

[32] Z. Yan, Higher-order topological insulators and superconductors, Acta Phys. Sin. **68**, 226101 (2019).

[33] F. Schindler, Dirac equation perspective on higher-order topological insulators, J. Appl. Phys. **128**, 221102 (2020).

[34] B. Xie, H.-X. Wang, X. Zhang, P. Zhan, J.-H. Jiang, M. Lu, and Y. Chen, Higher-order band topology, Nat. Rev. Phys. **3**, 520 (2021).

[35] D. Călugăru, V. Juričić, and B. Roy, Higher-order topological phases: A general principle of construction, Phys. Rev. B **99**, 041301(R) (2019).

[36] Y. Ren, Z. Qiao, and Q. Niu, Engineering Corner States from Two-Dimensional Topological Insulators, Phys. Rev. Lett. **124**, 166804 (2020).

[37] C. Chen, Z. Song, J.-Z. Zhao, Z. Chen, Z.-M. Yu, X.-L. Sheng, and S. A. Yang, Universal Approach to Magnetic Second-Order Topological Insulator, Phys. Rev. Lett. **125**, 056402 (2020).

[38] X. Huang, J. Lu, Z. Yan, M. Yan, W. Deng, G. Chen, and Z. Liu, Acoustic higher-order topology derived from first-order with built-in Zeeman-like fields, Sci. Bull **67**, 488 (2022).

[39] R. Jackiw and C. Rebbi, Solitons with fermion number 1/2, Phys. Rev. D **13**, 3398 (1976).

[40] S.-Q. Shen, *Topological Insulators: Dirac Equation in Condensed Matters*, Vol. 174 (Springer Science & Business Media, New York, 2013).

[41] X. Zhu, Tunable Majorana corner states in a two-dimensional second-order topological superconductor induced by magnetic fields, Phys. Rev. B **97**, 205134 (2018).

[42] Z.-Y. Zhuang and Z. Yan, Topological phase transitions and evolution of boundary states induced by Zeeman fields in second-order topological insulators, Front. Phys. **10**, 866347 (2022).

[43] R.-X. Zhang, W. S. Cole, and S. Das Sarma, Helical Hinge Majorana Modes in Iron-Based Superconductors, Phys. Rev. Lett. **122**, 187001 (2019).

[44] M. Kheirkhah, Z. Yan, and F. Marsiglio, Vortex-line topology in iron-based superconductors with and without second-order topology, Phys. Rev. B **103**, L140502 (2021).

[45] M. Kheirkhah, Z.-Y. Zhuang, J. Maciejko, and Z. Yan, Surface Bogoliubov-Dirac cones and helical Majorana hinge modes in superconducting Dirac semimetals, Phys. Rev. B **105**, 014509 (2022).

[46] C. W. Peterson, W. A. Benalcazar, T. L. Hughes, and G. Bahl, A quantized microwave quadrupole insulator with topologically protected corner states, Nature (London) **555**, 346 (2018).

[47] M. Serra-Garcia, V. Peri, R. Süsstrunk, O. R. Bilal, T. Larsen, L. G. Villanueva, and S. D. Huber, Observation of a phononic quadrupole topological insulator, Nature (London) **555**, 342 (2018).

[48] S. Imhof, C. Berger, F. Bayer, J. Brehm, L. W. Molenkamp, T. Kiessling, F. Schindler, C. H. Lee, M. Greiter, T. Neupert, and R. Thomale, Topolectrical-circuit realization of topological corner modes, Nat. Phys. **14**, 925 (2018).

[49] X. Zhang, H.-X. Wang, Z.-K. Lin, Y. Tian, B. Xie, M.-H. Lu, Y.-F. Chen, and J.-H. Jiang, Second-order topology and multidimensional topological transitions in sonic crystals, Nat. Phys. **15**, 582 (2019).

[50] X.-D. Chen, W.-M. Deng, F.-L. Shi, F.-L. Zhao, M. Chen, and J.-W. Dong, Direct Observation of Corner States in Second-Order Topological Photonic Crystal Slabs, Phys. Rev. Lett. **122**, 233902 (2019).

[51] H. Fan, B. Xia, L. Tong, S. Zheng, and D. Yu, Elastic Higher-Order Topological Insulator with Topologically Protected Corner States, Phys. Rev. Lett. **122**, 204301 (2019).

[52] A. El Hassan, F. K. Kunst, A. Moritz, G. Andler, E. J. Bergholtz, and M. Bourennane, Corner states of light in photonic waveguides, Nat. Photonics **13**, 697 (2019).

[53] F. Schindler, Z. Wang, M. G. Vergniory, A. M. Cook, A. Murani, S. Sengupta, A. Yu. Kasumov, R. Deblock, S. Jeon, I. Drozdov, *et al.*, Higher-order topology in bismuth, Nat. Phys. **14**, 918 (2018).

[54] M. J. Gray, J. Freudenstein, S. Y. F. Zhao, R. O'Connor, S. Jenkins, N. Kumar, M. Hoek, A. Kopec, S. Huh, T. Taniguchi, *et al.*, Evidence for helical hinge zero modes in an Fe-based superconductor, Nano Lett. **19**, 4890 (2019).

[55] Y.-B. Choi, Y. Xie, C.-Z. Chen, J. Park, S.-B. Song, J. Yoon, B. J. Kim, T. Taniguchi, K. Watanabe, J. Kim, *et al.*, Evidence of higher-order topology in multilayer WTe_2 from Josephson coupling through anisotropic hinge states, Nat. Mater. **19**, 974 (2020).

[56] R. Noguchi, M. Kobayashi, Z. Jiang, K. Kuroda, T. Takahashi, Z. Xu, D. Lee, M. Hirayama, M. Ochi, T. Shirasawa *et al.*, Evidence for a higher-order topological insulator in a three-dimensional material built from van der Waals stacking of bismuth-halide chains, Nat. Mater. **20**, 473 (2021).

[57] L. Aggarwal, P. Zhu, T. L. Hughes, and V. Madhavan, Evidence for higher order topology in Bi and $Bi_{0.92}$ $Sb_{0.08}$, Nat. Commun. **12**, 4420 (2021).

[58] N. Shumiya, M. S. Hossain, J.-X. Yin, Z. Wang, M. Litskevich, C. Yoon, Y. Li, Y. Yang, Y.-X. Jiang, G. Cheng *et al.*, Evidence of a room-temperature quantum spin Hall edge state in a higher-order topological insulator, Nat. Mater. **21**, 1111 (2022).

[59] D. Zhu, B.-X. Li, and Z. Yan, Sublattice-sensitive Majorana modes, Phys. Rev. B **106**, 245418 (2022).

[60] M. Kheirkhah, D. Zhu, J. Maciejko, and Z. Yan, Corner- and sublattice-sensitive Majorana zero modes on the kagome lattice, Phys. Rev. B **106**, 085420 (2022).

[61] A. Haim and Y. Oreg, Time-reversal-invariant topological superconductivity in one and two dimensions, Phys. Rep **825**, 1 (2019).

[62] C. Nayak, S. H. Simon, A. Stern, M. Freedman, and S. Das Sarma, Non-Abelian anyons and topological quantum computation, Rev. Mod. Phys. **80**, 1083 (2008).

[63] X.-J. Liu, Chris L. M. Wong, and K. T. Law, Non-Abelian Majorana Doublets in Time-Reversal-Invariant Topological Superconductors, Phys. Rev. X **4**, 021018 (2014).

[64] P. Gao, Y.-P. He, and X.-J. Liu, Symmetry-protected non-Abelian braiding of Majorana Kramers pairs, Phys. Rev. B **94**, 224509 (2016).

[65] C. Schrade and L. Fu, Quantum Computing with Majorana Kramers Pairs, Phys. Rev. Lett. **129**, 227002 (2022).

[66] R. Yu, W. Zhang, H.-J. Zhang, S.-C. Zhang, X. Dai, and Z. Fang, Quantized anomalous Hall effect in magnetic topological insulators, Science **329**, 61 (2010).

[67] A. H. Castro Neto, F. Guinea, N. M. R. Peres, K. S. Novoselov, and A. K. Geim, The electronic properties of graphene, Rev. Mod. Phys. **81**, 109 (2009).

[68] F. D. M. Haldane, Model for a Quantum Hall Effect without Landau Levels: Condensed-Matter Realization of the "Parity Anomaly", Phys. Rev. Lett. **61**, 2015 (1988).

[69] A. P. Schnyder, S. Ryu, A. Furusaki, and A. W. W. Ludwig, Classification of topological insulators and superconductors in three spatial dimensions, Phys. Rev. B **78**, 195125 (2008).

[70] A. Kitaev, Periodic table for topological insulators and superconductors, in *Advances in Theoretical Physics: Landau Memorial Conference*, edited by V. Lebedev and M. Feigel'man, AIP Conf. Proc. No. 1134 (AIP, New York, 2009), p. 22.

[71] S. Ryu, A. P. Schnyder, A. Furusaki, and A. W. W. Ludwig, Topological insulators and superconductors: Tenfold way and dimensional hierarchy, New J. Phys. **12**, 065010 (2010).

[72] L. Fu and C. L. Kane, Josephson current and noise at a superconductor/quantum-spin-Hall-insulator/superconductor junction, Phys. Rev. B **79**, 161408(R) (2009).

[73] Z. Yan, Majorana corner and hinge modes in second-order topological insulator/superconductor heterostructures, Phys. Rev. B **100**, 205406 (2019).

[74] B. Jäck, Y. Xie, J. Li, S. Jeon, B. A. Bernevig, and A. Yazdani, Observation of a Majorana zero mode in a topologically protected edge channel, Science **364**, 1255 (2019).

[75] Y.-J. Wu, J. Hou, Y.-M. Li, X.-W. Luo, X. Shi, and C. Zhang, In-Plane Zeeman-Field-Induced Majorana Corner and Hinge Modes in an *s*-Wave Superconductor Heterostructure, Phys. Rev. Lett. **124**, 227001 (2020).

[76] T. Liu, James Jun He, and F. Nori, Majorana corner states in a two-dimensional magnetic topological insulator on a high-temperature superconductor, Phys. Rev. B **98**, 245413 (2018).

[77] R.-X. Zhang, W. S. Cole, X. Wu, and S. Das Sarma, Higher-Order Topology and Nodal Topological Superconductivity in Fe(Se,Te) Heterostructures, Phys. Rev. Lett. **123**, 167001 (2019).

[78] X.-H. Pan, K.-J. Yang, L. Chen, G. Xu, C.-X. Liu, and X. Liu, Lattice-Symmetry-Assisted Second-Order Topological Superconductors and Majorana Patterns, Phys. Rev. Lett. **123**, 156801 (2019).

[79] M. Kheirkhah, Y. Nagai, C. Chen, and F. Marsiglio, Majorana corner flat bands in two-dimensional second-order topological superconductors, Phys. Rev. B **101**, 104502 (2020).

[80] K. Laubscher, D. Chughtai, D. Loss, and J. Klinovaja, Kramers pairs of Majorana corner states in a topological insulator bilayer, Phys. Rev. B **102**, 195401 (2020).

[81] B.-X. Li and Z. Yan, Boundary topological superconductors, Phys. Rev. B **103**, 064512 (2021).

[82] Y.-X. Li and T. Zhou, Rotational symmetry breaking and partial Majorana corner states in a heterostructure based on high-T_c superconductors, Phys. Rev. B **103**, 024517 (2021).

[83] Y. Tan, Z.-H. Huang, and X.-J. Liu, Two-particle Berry phase mechanism for Dirac and Majorana Kramers pairs of corner modes, Phys. Rev. B **105**, L041105 (2022).

[84] Y.-J. Wu, W. Tu, and N. Li, Majorana corner states in an attractive quantum spin Hall insulator with opposite in-plane Zeeman energy at two sublattice sites, J. Phys.: Condens. Matter **34**, 375601 (2022).

[85] Z. Wu, Z. Yan, and W. Huang, Higher-order topological superconductivity: Possible realization in Fermi gases and Sr_2RuO_4, Phys. Rev. B **99**, 020508(R) (2019).

[86] S. Ikegaya, W. B. Rui, D. Manske, and A. P. Schnyder, Tunable Majorana corner modes in noncentrosymmetric superconductors: Tunneling spectroscopy and edge imperfections, Phys. Rev. Research **3**, 023007 (2021).

[87] B. Roy, Higher-order topological superconductors in $\mathcal{P}$-, $\mathcal{T}$-odd quadrupolar dirac materials, Phys. Rev. B **101**, 220506(R) (2020).
[88] X. Zhu, Second-Order Topological Superconductors with Mixed Pairing, Phys. Rev. Lett. **122**, 236401 (2019).
[89] M. Kheirkhah, Z. Yan, Y. Nagai, and F. Marsiglio, First- and Second-Order Topological Superconductivity and Temperature-Driven Topological Phase Transitions in the Extended Hubbard Model with Spin-Orbit Coupling, Phys. Rev. Lett. **125**, 017001 (2020).
[90] J. Ahn and B.-J. Yang, Higher-order topological superconductivity of spin-polarized fermions, Phys. Rev. Research **2**, 012060(R) (2020).
[91] Y.-T. Hsu, W. S. Cole, R.-X. Zhang, and J. D. Sau, Inversion-Protected Higher-Order Topological Superconductivity in Monolayer WTe_2, Phys. Rev. Lett. **125**, 097001 (2020).
[92] T. Li, M. Geier, J. Ingham, and H. D. Scammell, Higher-order topological superconductivity from repulsive interactions in kagome and honeycomb systems, 2D Mater. **9**, 015031 (2022).
[93] H. D. Scammell, J. Ingham, M. Geier, and T. Li, Intrinsic first- and higher-order topological superconductivity in a doped topological insulator, Phys. Rev. B **105**, 195149 (2022).
[94] C. Zeng, T. D. Stanescu, C. Zhang, V. W. Scarola, and S. Tewari, Majorana Corner Modes with Solitons in an Attractive Hubbard-Hofstadter Model of Cold Atom Optical Lattices, Phys. Rev. Lett. **123**, 060402 (2019).
[95] Y. Volpez, D. Loss, and J. Klinovaja, Second-Order Topological Superconductivity in π-Junction Rashba Layers, Phys. Rev. Lett. **122**, 126402 (2019).
[96] S. Franca, D. V. Efremov, and I. C. Fulga, Phase-tunable second-order topological superconductor, Phys. Rev. B **100**, 075415 (2019).
[97] B. Huang, G. Luo, and N. Xu, Mirror-symmetry-protected topological superfluid and second-order topological superfluid in bilayer fermionic gases with spin-orbit coupling, Phys. Rev. A **100**, 023602 (2019).
[98] X. Wu, W. A. Benalcazar, Y. Li, R. Thomale, C.-X. Liu, and J. Hu, Boundary-Obstructed Topological High-T_c Superconductivity in Iron Pnictides, Phys. Rev. X **10**, 041014 (2020).
[99] Y.-B. Wu, G.-C. Guo, Z. Zheng, and X.-B. Zou, Effective Hamiltonian with tunable mixed pairing in driven optical lattices, Phys. Rev. A **101**, 013622 (2020).
[100] Y.-B. Wu, G.-C. Guo, Z. Zheng, and X.-B. Zou, Multiorder topological superfluid phase transitions in a two-dimensional optical superlattice, Phys. Rev. A **104**, 013306 (2021).
[101] S. Qin, C. Fang, F.-C. Zhang, and J. Hu, Topological Superconductivity in an Extended s-Wave Superconductor and its Implication to Iron-Based Superconductors, Phys. Rev. X **12**, 011030 (2022).
[102] B. Roy and V. Juričić, Mixed-parity octupolar pairing and corner Majorana modes in three dimensions, Phys. Rev. B **104**, L180503 (2021).
[103] S.-B. Zhang, W. B. Rui, A. Calzona, S.-J. Choi, A. P. Schnyder, and B. Trauzettel, Topological and holonomic quantum computation based on second-order topological superconductors, Phys. Rev. Research **2**, 043025 (2020).
[104] S.-B. Zhang, A. Calzona, and Björn Trauzettel, All-electrically tunable networks of Majorana bound states, Phys. Rev. B **102**, 100503(R) (2020).
[105] T. E. Pahomi, M. Sigrist, and A. A. Soluyanov, Braiding Majorana corner modes in a second-order topological superconductor, Phys. Rev. Research **2**, 032068(R) (2020).
[106] C.-C. Liu, W. Feng, and Y. Yao, Quantum Spin Hall Effect in Silicene and Two-Dimensional Germanium, Phys. Rev. Lett. **107**, 076802 (2011).
[107] C.-C. Liu, H. Jiang, and Y. Yao, Low-energy effective Hamiltonian involving spin-orbit coupling in silicene and two-dimensional germanium and tin, Phys. Rev. B **84**, 195430 (2011).
[108] M. Ezawa, Valley-Polarized Metals and Quantum Anomalous Hall Effect in Silicene, Phys. Rev. Lett. **109**, 055502 (2012).
[109] F. Wu, T. Lovorn, E. Tutuc, I. Martin, and A. H. MacDonald, Topological Insulators in Twisted Transition Metal Dichalcogenide Homobilayers, Phys. Rev. Lett. **122**, 086402 (2019).
[110] M.-H. Zare and H. Mosadeq, Spin liquid in twisted homobilayers of group-VI dichalcogenides, Phys. Rev. B **104**, 115154 (2021).
[111] A. Luo, Z. Song, and G. Xu, Fragile topological band in the checkerboard antiferromagnetic monolayer FeSe, npj Comput. Mater. **8**, 26 (2022).
[112] H. Mu, G. Zhao, H. Zhang, and Z. Wang, Antiferromagnetic second-order topological insulator with fractional mass-kink, npj Comput. Mater. **8**, 82 (2022).
[113] J. A. Stroscio and D. M. Eigler, Atomic and molecular manipulation with the scanning tunneling microscope, Science **254**, 1319 (1991).
[114] O. Custance, R. Perez, and S. Morita, Atomic force microscopy as a tool for atom manipulation, Nat. Nanotechnol. **4**, 803 (2009).
[115] W. P. Su, J. R. Schrieffer, and A. J. Heeger, Solitons in Polyacetylene, Phys. Rev. Lett. **42**, 1698 (1979).